Level set distribution model of nested structures using logarithmic transformation

Atsushi Saito [a,*], Masaki Tsujikawa [a], Tetsuya Takakuwa [b], Shigehito Yamada [b], Akinobu Shimizu [a]

[a] *Tokyo University of Agriculture and Technology, 2-24-16 Nakacho, Koganei, Tokyo 184-8588, Japan*
[b] *Kyoto University, Yoshida-honmachi, Sakyo-ku, Kyoto 606-8501, Japan*

ABSTRACT

In this study, we propose a method for constructing a multishape statistical shape model (SSM) for nested structures such that each is a subset or superset of another. The proposed method has potential application to any pair of shapes with an inclusive relationship. These types of shapes are often found in anatomy, such as the brain surface and ventricles. The main contribution of this paper is to introduce a new shape representation called log-transformed level set function (LT-LSF), which has a vector space structure that preserves the correct inclusive relationship of the nested shape. In addition, our method is applicable to an arbitrary number of nested shapes. We demonstrate the effectiveness of the proposed shape representation by modeling the anatomy of human embryos, including the brain, ventricles, and choroid plexus volumes. The performance of the SSM was evaluated in terms of generalization and specificity ability. Additionally, we measured leakage criteria to assess the ability to preserve inclusive relationships. A quantitative comparison of our SSM with conventional multishape SSMs demonstrates the superiority of the proposed method.

© 2019 Elsevier B.V. All rights reserved.

1. Introduction

Statistical shape models (SSMs) of anatomy are one of the most important tools for medical image analysis, especially for automated image segmentation. SSMs provide good constraints on automated image segmentation algorithms, and an accurate SSM is important for improving segmentation performance. Key issues for improving the performance of SSMs include the choice of shape representation and statistical analysis method.

Many researchers have attempted to describe shapes using various methods, which are categorized as explicit and implicit. The most common approach in explicit methods is a point distribution model (PDM) (Cootes et al., 1995), which represents a shape as a set of coordinates of the landmarks on the surface. Medial representation (*m*-rep) developed by Yushkevich et al. (2003) is also a popular explicit model, where the object is represented by the center lines and the corresponding radii, which leads to a more compact description for a specific shape. This representation was later extended as *s*-rep (Pizer et al., 2013), which describes not only the object boundary but also its interior. In these methods, there are

a number of options for placing landmarks and establishing point correspondences between different subjects, as shown in a comprehensive review by Heimann and Meinzer (2009). Among the implicit methods, the level set distribution model (LSDM) is the most popular approach. The LSDM has the advantage that it does not require point correspondences between different subjects, and it is often applied to segmentation using various approaches, such as the level set method (Cremers et al., 2007) and graph cuts (Saito et al., 2017).

The multishape SSM has been a growing research topic in recent years. The main concept of the multishape SSM is to encode the relationship between neighboring structures, which is helpful to improve the performance of multishape segmentation. Several researchers have proposed multishape SSMs using both PDM (Duta and Sonka, 1998; Okada et al., 2015) and LSDM (Tsai et al., 2004; Jing et al., 2004; Saito et al., 2013). Duta and Sonka (1998) proposed a simple extension of PDM for 10 neuroanatomic structures in brain MR images. Wang et al. (2012) proposed PDM for multiple organs in mouse micro-CT images, in which a conditional Gaussian model was used to describe the shape correlations between different organs. Okada et al. (2015) also developed a multishape PDM for eight abdominal organs whose relationships with neighboring organs were modeled via an organ correlation graph. LSDM was also extended to multiple shapes by Tsai et al. (2004),

Jing et al. (2004) and Saito et al. (2013). Tsai et al. (2004) proposed a simple extension of LSDM for three brain structures by applying statistical analysis to the concatenated level set functions (LSFs). Jing et al. (2004) modeled the differences in the LSFs of neighboring shapes and applied this to a neighbor-constrained segmentation algorithm. Saito et al. (2013) constructed a hierarchical SSM for 14 organs from 27 cases utilizing a synthesis-based learning algorithm to overcome the lack of a training dataset. The methods mentioned above have a potential risk of creating anatomically incorrect overlaps between neighboring organs. Recently, other implicit models using probabilistic shape representations were developed to describe multiple shapes (Pohl et al., 2007; Malcolm et al., 2008; Changizi and Hamarneh, 2010), in which the class with the highest probability is assigned to each voxel. Such one-label-per-voxel descriptions can intrinsically rule out organ overlaps. Pohl et al. (2007) proposed a logarithm of odds (LogOdds)-based shape representation that embeds multiple LSFs into a vector space and relates them to probabilistic atlases (PAs). Malcolm et al. (2008) presented a label space that is a mapping of class labels to vertices on a regular simplex, which forms the basis of a convex linear structure. Changizi and Hamarneh (2010) proposed a bijective mapping of such a simplex to the Euclidean real space using isometric log ratio (ILR) transformation to improve the performance of the principal component analysis (PCA).

Nesting of structures is an interesting subject in the field of statistical multishape modeling because it is often found in anatomy, e.g., in the brain surface and ventricle and in the bones and their medullary cavities. In principle, most existing techniques can be applied or extended to represent nested shapes. For example, Frangi et al. (2002) developed a PDM of nested shapes including the outer surface of the left myocardium and the blood pool inside it. However, shapes generated from this model are not guaranteed to have a correct inclusive relationship. One potential approach to overcome this issue is to represent shapes by diffeomorphic transformation of a shape template (Durrleman et al., 2014; Fishbaugh et al., 2017). However, diffeomorphic setting is too strict and not suitable for complicated shapes that might have topological changes, e.g., topological change might occur in the choroid plexus of the human embryo due to development (see Fig. 8). As far as we know, our previous model (Saito et al., 2017) is the first SSM that guarantees a correct inclusive relationship and flexibility for topological changes. Different shapes are represented using different level surfaces of a single LSF. The basic idea is similar to the multilayer level set method (Chung and Vese, 2009; Liu et al., 2016; Yang et al., 2017), which is used for segmentation purposes only. However, this method (Saito et al., 2017) has been demonstrated only for two nested objects. Moreover, we found that this shape representation forms a highly skewed distribution (see Section 4), and the SSM constructed by standard PCA may have poor performance.

In this study, we propose an SSM for nested shapes using a new shape representation using logarithmic transformation of LSFs; we refer to it as the LT-LSF method. The main goal of this study is to define a mapping of a nested shape onto a vector space that preserves the nesting relationship. We compared the proposed method with some of the most related ones (Tsai et al., 2004; Pohl et al., 2007; Saito et al., 2017), all of which are implicit multishape representation methods. Comparison with the SSM proposed by Jing et al. (2004) is outside the scope of this study because it is not a simultaneous model. The main contributions of the proposed method compared to conventional methods are summarized as follows.

1. The proposed shape representation method preserves inclusive relationships, which is different to other studies (Tsai et al., 2004; Pohl et al., 2007), except for (Saito et al., 2017).

2. The proposed method can naturally be extended to an arbitrary number of nested shapes in an arbitrary number of dimensions. We demonstrated this concept by constructing three nesting structures, whereas a previous study (Saito et al., 2017) only used two nested objects.
3. The proposed method achieved higher performance than conventional ones (Tsai et al., 2004; Pohl et al., 2007; Saito et al., 2017).

The proposed method was applied to the statistical shape modeling of 38 cases of human embryos derived from the Kyoto Collection of Human Embryos (Yamaguchi and Yamada, 2018). Embryonic brain is a good choice for a proof of concept of our method because it poses the following challenges: (i) the shape is three-dimensional, (ii) it has three nested structures (i.e., brain, ventricle, and choroid plexus), and (iii) topological changes occur. A quantitative comparison of the performance of the proposed SSM to conventional SSMs demonstrated the effectiveness of the proposed method.

2. Methods

2.1. Level-set-based shape representation

First, we introduce the basics of the level-set-based shape representation. Let $\Omega \subset \mathbb{R}^d$ be a bounded open image domain and $\mathbb{S}$ denote all the possible open subsets of Ω. Shape is defined as a member of $\mathbb{S}$. Let us denote $\phi_S : \Omega \to \mathbb{R}$ as the signed distance function of the shape $S \in \mathbb{S}$ that maps a point $\mathbf{r} \in \Omega$ to the distance from the surface ∂S multiplied by -1 inside the shape and $+1$ elsewhere:

$$\phi_S(\mathbf{r}) = \begin{cases} -\min_{\mathbf{s} \in \partial S} \|\mathbf{r} - \mathbf{s}\| & \text{if } \mathbf{r} \in S \\ +\min_{\mathbf{s} \in \partial S} \|\mathbf{r} - \mathbf{s}\| & \text{if } \mathbf{r} \in \Omega \setminus S \end{cases}. \tag{1}$$

Although Eq. (1) cannot be defined for the special cases $S = \emptyset$ and $S = \Omega$, neither of these cases occur in practice, so they are not considered in this study. The shape is embedded as the sublevel set of the function $\phi_S(\mathbf{r})$, i.e.,

$$S = \{\mathbf{r} \in \Omega \,|\, \phi_S(\mathbf{r}) < 0\}. \tag{2}$$

In practice, the signed distance function $\phi_S(\mathbf{r})$ is discretized at the voxel level, and we only need to calculate the value of the grid points on the image coordinates $\{\mathbf{r}_1, \ldots, \mathbf{r}_p\} \in \Omega$. The signed distance function on the grid points can efficiently be calculated by the Euclidean distance transform algorithm (Saito and Toriwaki, 1994).

2.2. Nested objects

This section introduces the class of nested objects. Suppose we have two shapes $S_1, S_2 \in \mathbb{S}$. The required properties for the shape pair (S_1, S_2) to be nested are that (i) one shape is a subset of the other ($S_1 \subset S_2$) and (ii) their boundaries do not contact one another ($\partial S_1 \cap \partial S_2 = \emptyset$), that is, in short, the closure of S_1 is a subset of S_2 (i.e., $S_1 \cup \partial S_1 \subset S_2$). To borrow the term from Hormander (1973), this is also referred to as "S_1 is relatively compact in S_2" and is denoted as $S_1 \Subset S_2$. This concept can be generalized to an arbitrary number of objects. The class of a set of n-nested shapes $\mathbb{T}_n$ ($n \geq 2$) is expressed as

$$\mathbb{T}_n = \{(S_1, S_2, \ldots, S_n) \in \mathbb{S}^n \,|\, S_1 \Subset S_2 \Subset \cdots \Subset S_n\}. \tag{3}$$

Note that this definition includes some special cases, e.g., $\{(\emptyset, \emptyset), (\emptyset, \Omega), (\Omega, \Omega)\} \subset \mathbb{T}_2$.

Fig. 1 illustrates which kind of shapes are the valid nested objects in this study. It should be noted that shapes in Fig. 1 (b) are nested because their boundaries ∂S_i ($i \in \{1, 2\}$) do not include the image boundary $\partial \Omega$.
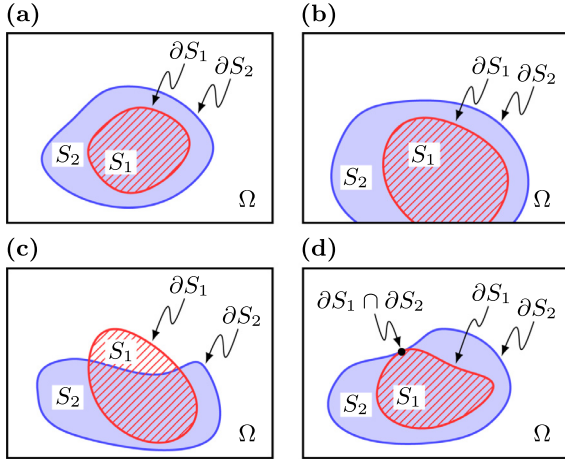
Fig. 1. Typical examples of nested shapes ((a) and (b)) and a non-nested shape ((c) and (d)). From the definition, the pair of shapes in (a) is nested. (b) shows another type of nested shape adjoining the boundary of the image domain Ω. Although (d) also satisfies $S_1 \subset S_2$, the shapes are not nested because $S_1 \cap S_2 \neq \emptyset$.

2.3. Proposed shape representation (LT-LSF)

In this section, we describe the new shape representation function called LT-LSF. It is an important fact that signed distance functions $(\phi_{S_1}, \ldots, \phi_{S_n})$ associated with the nested shapes $S = (S_1, \ldots, S_n) \in \mathbb{T}_n$ monotonically decrease with respect to the nesting level, i.e.,

$$\phi_{S_1}(\mathbf{r}) > \ldots > \phi_{S_n}(\mathbf{r}) \quad \forall \mathbf{r} \in \Omega. \tag{4}$$

The proof of this can be derived from Eq. (1) (see Corollary 1 in Appendix A). Another important fact is that the reverse is also true. Suppose we have n continuous real-valued functions $\varphi_i : \Omega \to \mathbb{R}$ (which could be signed distance functions) and their sublevel sets $S_i = \{\mathbf{r} \in \Omega | \varphi_i(\mathbf{r}) < 0\}$, where $i \in \{1, \ldots, n\}$, respectively. Then, the condition $\varphi_1(\mathbf{r}) > \ldots > \varphi_n(\mathbf{r}) \; \forall \mathbf{r} \in \Omega$ is the sufficient condition for the shapes to be nested, i.e., $(S_1, \ldots, S_n) \in \mathbb{T}_n$ (see Corollary 2 in Appendix A).

For given nested shapes $S = (S_1, \ldots, S_n) \in \mathbb{T}_n$, let us consider the vector-valued function that consists of the level set function values $\boldsymbol{\phi}_S(\mathbf{r}) = [\phi_{S_1}(\mathbf{r}), \ldots, \phi_{S_n}(\mathbf{r})]^T$ at position $\mathbf{r} \in \Omega$. Recall that entries in $\boldsymbol{\phi}_S(\mathbf{r})$ are arranged in decreasing order (cf. Eq. (4)), so $\boldsymbol{\phi}_S(\mathbf{r})$ is a member of a subset of n-dimensional vectors $\mathcal{X}_n \subset \mathbb{R}^n$ composed of all the possible vectors $\boldsymbol{v} = [v_1, \ldots, v_n]^T$ having elements sorted in descending order, i.e.,

$$\mathcal{X}_n = \{\boldsymbol{v} \in \mathbb{R}^n \,|\, v_1 > \cdots > v_n\}. \tag{5}$$

The space $\mathcal{X}_n$ is not closed under the linear operations because, for example, $\boldsymbol{v} \in \mathcal{X}_n \Rightarrow -\boldsymbol{v} \notin \mathcal{X}_n$. This implies that shapes produced by principal component analysis (PCA) on $\mathcal{X}_n$ may not preserve nesting structures. To overcome this issue, we introduce a homeomorphism between $\mathcal{X}_n$ and a vector space $\mathbb{R}^n$ on which PCA is applicable without issues.

Because the condition in Eq. (5) corresponds to the system of $(n-1)$ linear inequalities $v_i - v_{i+1} > 0 \forall i \in \{1, \ldots, n-1\}$, Eq. (5) can be rewritten as

$$\mathcal{X}_n = \{\boldsymbol{v} \in \mathbb{R}^n \,|\, A\boldsymbol{v} > \mathbf{0}\} \tag{6}$$

where A is the $(n-1) \times n$ matrix whose (i, j) element is

$$A_{i,j} = \begin{cases} 1 & \text{if } i = j \\ -1 & \text{if } i = j - 1 \,. \\ 0 & else \end{cases} \tag{7}$$

This matrix has rank $(n-1)$. We introduce an n-dimensional row vector of all ones $\boldsymbol{b} = \mathbb{1}^{1 \times n}$ that is perpendicular to all the rows

in A to build a full rank matrix $\begin{bmatrix} A \\ \boldsymbol{b} \end{bmatrix} \in \mathbb{R}^{n \times n}$. Using this matrix, we can consider an invertible linear transformation $\begin{bmatrix} A \\ \boldsymbol{b} \end{bmatrix} \boldsymbol{v} = \begin{bmatrix} A\boldsymbol{v} \\ \boldsymbol{b}\boldsymbol{v} \end{bmatrix}$. Recall that the subvector $A\boldsymbol{v}$ has only positive elements (cf. Eq. (6)), while the last element $\boldsymbol{b}\boldsymbol{v}$ can be any real number. Using the logarithmic operation on the first $(n-1)$ elements $A\boldsymbol{v}$, we can define a one-to-one mapping $\boldsymbol{f} : \mathcal{X}_n \to \mathbb{R}^n$:

$$\boldsymbol{f}(\boldsymbol{v}) = \begin{bmatrix} \log[A\boldsymbol{v}] \\ \boldsymbol{b}\boldsymbol{v} \end{bmatrix} \tag{8}$$

where we denote $\log[\cdot]$ as an elementwise logarithmic function. Finally, the proposed shape representation for the nested shapes $S \in \mathbb{T}_n$ can be written as $\boldsymbol{f} \circ \boldsymbol{\phi}_S$. The inverse mapping from $\boldsymbol{u} \in \mathbb{R}^n$ to $\boldsymbol{f}^{-1}(\boldsymbol{u}) \in \mathcal{X}_n$ is defined as

$$\boldsymbol{f}^{-1}(\boldsymbol{u}) = \begin{bmatrix} A \\ \boldsymbol{b} \end{bmatrix}^{-1} \begin{bmatrix} [\exp u_1, \ldots, \exp u_{n-1}]^T \\ u_n \end{bmatrix}. \tag{9}$$

By borrowing the vector space structure $\mathbb{R}^n$ using the invertible mapping $\boldsymbol{f}$, we can define an addition operation $\oplus$ and a scalar multiplication operation $\circledast$ that are closed in $\mathcal{X}_n$. For $\boldsymbol{v}, \boldsymbol{v}' \in \mathcal{X}_n$ and $\alpha \in \mathbb{R}$, we have

$$\boldsymbol{v} \oplus \boldsymbol{v}' \equiv \boldsymbol{f}^{-1}(\boldsymbol{f}(\boldsymbol{v}) + \boldsymbol{f}(\boldsymbol{v}')) = \begin{bmatrix} A \\ \boldsymbol{b} \end{bmatrix}^{-1} \begin{bmatrix} (A\boldsymbol{v}) \odot (A\boldsymbol{v}') \\ \boldsymbol{b}(\boldsymbol{v} + \boldsymbol{v}') \end{bmatrix} \tag{10}$$

$$\alpha \circledast \boldsymbol{v} \equiv \boldsymbol{f}^{-1}(\alpha * \boldsymbol{f}(\boldsymbol{v})) = \begin{bmatrix} A \\ \boldsymbol{b} \end{bmatrix}^{-1} \begin{bmatrix} (A\boldsymbol{v})^{\circ \alpha} \\ \alpha \cdot \boldsymbol{b}\boldsymbol{v} \end{bmatrix} \tag{11}$$

where we denote $\odot$ and $(\cdot)^{\circ \alpha}$ as elementwise multiplication and power operations, respectively. The algebraic structure $(\mathcal{X}_n, \oplus, \circledast)$ is a vector space because it is equivalent to a vector space $(\mathbb{R}^n, +, *)$ associated by a homeomorphic mapping $\boldsymbol{f}$. Using these operations, we can calculate an addition and scalar multiplication between vector-valued functions $\boldsymbol{\phi}_S(\mathbf{r})$ and $\boldsymbol{\phi}_{S'}(\mathbf{r})$ for nested shapes $S, S' \in \mathbb{T}_n$ as $(\boldsymbol{\phi}_S \oplus \boldsymbol{\phi}_{S'})(\mathbf{r})$ and $\alpha \circledast \boldsymbol{\phi}_{S'}(\mathbf{r})$, respectively.

2.4. Statistical analysis of nested shapes

The SSM is constructed by establishing a parametric model of the vector-valued function $\boldsymbol{f}(\boldsymbol{\phi}_S(\mathbf{r}))$. In practice, the function value $\boldsymbol{f}(\boldsymbol{\phi}_S(\mathbf{r}))$ is defined on the image grid points $\{\mathbf{r}_1, \ldots, \mathbf{r}_p\} \in \Omega$ and is represented as a vector in $\boldsymbol{x}_S \in \mathbb{R}^{np}$:

$$\boldsymbol{x}_S = \begin{bmatrix} \mathcal{D}[f_1(\boldsymbol{\phi}_S(\cdot))] \\ \vdots \\ \mathcal{D}[f_n(\boldsymbol{\phi}_S(\cdot))] \end{bmatrix} \tag{12}$$

where $\mathcal{D}[\chi(\cdot)] = [\chi(\mathbf{r}_1), \ldots, \chi(\mathbf{r}_p)]^T$ denotes the vectorization of the function $\chi(\cdot)$ by sampling on the grid points, and $f_i(\cdot)$ denotes the ith component of the function $\boldsymbol{f}(\cdot)$.

For the statistical shape analysis on the level set functions, it has been reported by Uchida et al. (2010) that PCA with spatial (or variable) weights can improve the generalization and specificity (Styner et al., 2003) of the SSM. Suppose we have a set of training nested shapes $\mathcal{T}_{\text{train}} \subset \mathbb{T}_n$. The weighting function for the shape of the ith layer is given as

$$w^{(i)}(\mathbf{r}) = \frac{1}{|\mathcal{T}_{\text{train}}|} \sum_{S \in \mathcal{T}_{\text{train}}} \frac{1}{1 + \exp\left(\gamma^{-1} \left|\boldsymbol{\phi}_{S_i}(\mathbf{r})\right|\right)}. \tag{13}$$

An example of the weight is displayed in Fig. 2. In this study, we extend this weight for the nested shape representation. Let $W^{(i)} = diag(\mathcal{D}[w^{(i)}(\cdot)])$ be the weight matrix for the shape of the ith nesting level. The basic plan for extending this weight to our nested shape representation is to add $W^{(j)}$ to the ith diagonal block
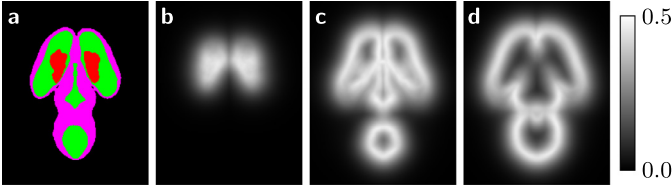
Fig. 2. Example of a training label and the weights. (a) shows a typical example of the training nested shape label. (b), (c), and (d) show the spatial weight $w^{(1)}$, $w^{(2)}$, and $w^{(3)}$, respectively.

if the function $f_i(\boldsymbol{\phi}_S)$ consists of the ith level set function ϕ_{S_i}, i.e.,

$$W = diag\left(W^{(1)} + W^{(2)}, \ldots, W^{(n-1)} + W^{(n)}, \lambda \sum_{i=1}^{n} W^{(i)}\right) \quad (14)$$

where γ is the parameter to adjust the variance.

Applying weighted PCA, we obtain the best approximation of the weighted training data $\{W\boldsymbol{x}_S\}_{S \in \mathcal{T}_{\text{train}}}$ in the form of

$$W\boldsymbol{x}_S \approx \boldsymbol{\mu} + U\Lambda^{\frac{1}{2}}\boldsymbol{\alpha}_S \quad (15)$$

where $\boldsymbol{\mu}$ denotes the average vector, $U = [\boldsymbol{u}_1, \ldots, \boldsymbol{u}_m]$ is the matrix whose columns are the first m principal modes, $\Lambda = diag(\sigma_1^2, \ldots, \sigma_m^2)$ is the diagonal matrix of the corresponding variances, and $\boldsymbol{\alpha}_S \in \mathbb{R}^m$ is the principal component vector. An arbitrary shape can be generated by $\boldsymbol{x} = W^{-1}\left(\boldsymbol{\mu} + U\Lambda^{\frac{1}{2}}\boldsymbol{\alpha}\right)$ under the assumption of unit m-dimensional normal distribution $\boldsymbol{\alpha} \sim \mathcal{N}_m(0, 1)$.

2.5. Relationship with the other shape representations

This section is an overview of the relationship between the proposed shape representation (LT-LSF) and the conventional ones: (i) multi-LSF (Tsai et al., 2004), (ii) RT-LSF (Saito et al., 2017), and (iii) LogOdds (Pohl et al., 2007). Note that we introduce a different weighting matrix W individually optimized for each shape representation $\boldsymbol{x}_S$.

2.5.1. Multi-LSF

This is the simplest shape representation method employed in Tsai et al. (2004) that is applicable to any type of multishape SSM. PCA is directly applied on the vector

$$\boldsymbol{x}_S = \begin{bmatrix} \mathcal{D}[\phi_{S_1}(\cdot)] \\ \vdots \\ \mathcal{D}[\phi_{S_n}(\cdot)] \end{bmatrix} \quad (16)$$

using the weight

$$W = diag\left(W^{(1)}, \ldots, W^{(n)}\right) \quad (17)$$

Note that this representation does not guarantee the nesting relationship.

2.5.2. RT-LSF

Saito et al. (2017) proposed the embedding of nested shapes into multiple-level contours of a single continuous real-valued function generated by rational transformation (RT) on LSFs, which we refer to as the RT-LSF method.[1] In this paper, we provide a more general formulation. For arbitrary nested shapes $S = (S_1, \ldots, S_n) \in \mathbb{T}_n$, there exists a function $\psi_S : \Omega \to \mathbb{R}$ that satisfies

$$S_i = \{\mathbf{r} \in \Omega \mid \psi_S(\mathbf{r}) < t_i\} \quad \forall i \in \{1, \ldots, n\} \, \forall \mathbf{r} \in \Omega \quad (18)$$

---

[1] In the original paper (Saito et al., 2017), this method was called single-LSF.

where $t_1 < t_2 < \cdots < t_n$ are predefined thresholds. One example of such a function is derived from the signed distance functions. For $n = 2$, the function is written as $\psi_S(\mathbf{r}) = \psi_S^{1,2}(\mathbf{r})$, where

$$\psi_S^{i,j}(\mathbf{r}) = \frac{t_j\phi_{S_i}(\mathbf{r}) - t_i\phi_{S_j}(\mathbf{r})}{\phi_{S_i}(\mathbf{r}) - \phi_{S_j}(\mathbf{r})} \quad (19)$$

Note that Eq. (19) can be interpreted as a section formula that divides t_i and t_j in the ratio $\phi_{S_i}(\mathbf{r}) : -\phi_{S_j}(\mathbf{r})$, i.e.,

$$\psi_S^{i,j}(\mathbf{r}) - t_i : t_j - \psi_S^{i,j}(\mathbf{r}) = \phi_{S_i}(\mathbf{r}) : -\phi_{S_j}(\mathbf{r}). \quad (20)$$

This function can be generalized to an arbitrary number of shapes $S \in \mathbb{T}_n$ $(n \geq 2)$ by combining $(n-1)$-functions $\left\{\psi_S^{1,2}, \psi_S^{2,3}, \ldots, \psi_S^{n-1,n}\right\}$ in a piecewise manner:

$$\psi_S(\mathbf{r}) = \begin{cases} \psi_S^{1,2}(\mathbf{r}) & \text{if } \mathbf{r} \in S_2 \\ \psi_S^{2,3}(\mathbf{r}) & \text{else if } \mathbf{r} \in S_3 \\ \vdots & \vdots \\ \psi_S^{n-2,n-1}(\mathbf{r}) & \text{else if } \mathbf{r} \in S_{n-1} \\ \psi_S^{n-1,n}(\mathbf{r}) & \text{elsewhere} \end{cases} \quad (21)$$

Saito et al. (2017) suggested that instead of applying PCA directly on $\psi_S(\mathbf{r})$, considering the monotonic transformation

$$h(\nu) = \begin{cases} (t_1 - t_{LB})\varsigma\left(\frac{\nu - t_1}{t_1 - t_{LB}}\right) + t_1 & \text{if } \nu < t_1 \\ \nu & \text{if } t_1 \leq \nu < t_n \\ (t_{UB} - t_n)\varsigma\left(\frac{\nu - t_n}{t_{UB} - t_n}\right) + t_n & \text{if } t_n \leq \nu \end{cases} \quad (22)$$

and applying PCA on $h(\psi_S(\mathbf{r}))$ yields better SSM. Here, $\varsigma(\nu)$ is a sigmoid function with $\varsigma'(0) = 1$ having two asymptotes $\lim_{\nu \to \pm\infty} \varsigma(\nu) = \pm 1$ ($\varsigma(\nu) = \tanh(\nu)$ is used in this study). The parameters t_{UB} and t_{LB} are the upper and the lower bounds of the sigmoid curve, respectively. Note that this is a generalized version of the one employed in Saito et al. (2017). Finally, PCA is performed on the vector

$$\boldsymbol{x}_S = \mathcal{D}[h(\psi_S(\cdot))] \quad (23)$$

with the weight

$$W = \sum_{i=1}^{n} W^{(i)}. \quad (24)$$

2.5.3. LogOdds

The LogOdds method (Pohl et al., 2007) is a probabilistic shape representation. Suppose we have $p_i(\mathbf{r}) i \in \{1, \ldots, n+1\}$ representing the probability that voxel $\mathbf{r} \in \Omega$ belongs to the ith class. The class label $L(\mathbf{r}) \in \{1, \ldots, n+1\}$ is assigned by calculating the class number with the maximum probability

$$L(\mathbf{r}) = \arg\max_{i \in \{1, \ldots, n+1\}} p_i(\mathbf{r}). \quad (25)$$

This method is designed to represent non-overlapping regions. To extend this method to represent nested shapes $S = (S_1, \ldots, S_n) \in \mathbb{T}_n$, we consider a tuple of regions $R = (R_1, R_2, \ldots, R_{n+1}) = (S_1, S_2 \setminus S_1, \ldots, S_n \setminus S_{n-1}, \Omega \setminus S_n)$, which compose mutually exclusive and collectively exhaustive sets of Ω (i.e., $\bigcup_{i=1}^{n+1} R_i = \Omega$ and $R_i \cap R_j = \emptyset$ for all i and j $i \neq j$). Let $L_S(\mathbf{r})$ be the class label associated with $S \in \mathbb{T}_n$ that satisfies

$$R_i = \{\mathbf{r} \in \Omega \mid L_S(\mathbf{r}) = i\}. \quad (26)$$

Because there exists a relationship $S_i = \bigcup_{j=1}^{i} R_j$, we have

$$S_i = \{\mathbf{r} \in \Omega \mid L_S(\mathbf{r}) \leq i\} \quad (27)$$

for $i = \{1, \ldots, n\}$.

Let $\boldsymbol{p}(\mathbf{r}) = [p_1(\mathbf{r}), \ldots, p_{n+1}(\mathbf{r})]^T \in \mathbb{P}_{n+1}$ be a vector of the probability, where

$$\mathbb{P}_{n+1} := \left\{\boldsymbol{p} \in (0, 1)^{n+1} \mid \sum_{i=1}^{n+1} p_i = 1\right\} \quad (28)$$

is an open probability simplex in an n-dimensional space because the $(n + 1)$th entry is calculated from the first n entries, i.e., $p_{n+1} = 1 - \sum_{i=1}^{n} p_i$. It is known that $\mathbb{P}_{n+1}$ has a surjective mapping $logit(\cdot) : \mathbb{P}_{n+1} \to \mathbb{R}^n$ defined as the logarithm of the ratio between the ith and the last entry of $\boldsymbol{p}(\mathbf{r})$. The ith entry of $\boldsymbol{t}(\mathbf{r}) = logit(\boldsymbol{p}(\mathbf{r}))$ is defined as

$$t_i(\mathbf{r}) := [logit(\boldsymbol{p}(\mathbf{r}))]_i = \log\left(\frac{p_i(\mathbf{r})}{p_{n+1}(\mathbf{r})}\right) \quad (29)$$

for $i \in \{1, \ldots, n + 1\}$. An important property for the LogOdds space $\{logit(\boldsymbol{p}) \mid \boldsymbol{p} \in \mathbb{P}_{p+1}\}$ is that it forms a vector space. The inverse mapping $\mathcal{P}$ of $\boldsymbol{t} \in \mathbb{R}^n$ back to the probability simplex is the generalized logistic function

$$[\mathcal{P}(\boldsymbol{t}(\mathbf{r}))]_i = \begin{cases} \frac{\exp(t_i)}{Z}, & \text{for } i \in \{1, \ldots, n\} \\ \frac{1}{Z}, & \text{if } i = n + 1 \end{cases} \quad (30)$$

where $Z = 1 + \sum_{i=1}^{n} e^{t_i}$ is the normalization factor. Combining Eqs. (30) and (25), we have the direct formula to calculate the class label from the LogOdds map:

$$L(\mathbf{r}) = \underset{i \in \{1, \ldots, n+1\}}{\arg\max} [\mathcal{P}(\boldsymbol{t}(\mathbf{r}))]_i = \underset{i \in \{1, \ldots, n+1\}}{\arg\max} \begin{bmatrix} \boldsymbol{t}(\mathbf{r}) \\ 0 \end{bmatrix}_i. \quad (31)$$

In this study, we assume that the probability is defined using the exponentiation of the signed distance function as

$$p_i(\mathbf{r}) = \frac{\exp(-\beta \cdot \phi_{R_i}(\mathbf{r}))}{\sum_{j=1}^{n+1} \exp(-\beta \cdot \phi_{R_j}(\mathbf{r}))} \quad (32)$$

with a positive constant $\beta > 0$. From Eqs. (30) and (32), we get

$$t_i(\mathbf{r}) := [logit(\boldsymbol{p}(\mathbf{r}))]_i = \beta(\phi_{R_{n+1}}(\mathbf{r}) - \phi_{R_i}(\mathbf{r})) \quad (33)$$

Since multiplication by a constant β does not affect the result of PCA, we set $\beta = 1$. Finally, from the fact that $\phi_{R_1}(\mathbf{r}) = \phi_{S_1}(\mathbf{r})$, $\phi_{R_i}(\mathbf{r}) = -\min(\phi_{S_i}(\mathbf{r}), -\phi_{S_{i+1}}(\mathbf{r}))$ for $1 \leq i \leq n$ and $\phi_{R_{n+1}}(\mathbf{r}) = -\phi_{S_n}(\mathbf{r})$, we get

$$\boldsymbol{t}(\mathbf{r}) = \begin{bmatrix} -\phi_{S_1}(\mathbf{r}) \\ \min(\phi_{S_1}(\mathbf{r}), -\phi_{S_2}(\mathbf{r})) \\ \vdots \\ \min(\phi_{S_{n-1}}(\mathbf{r}), -\phi_{S_n}(\mathbf{r})) \end{bmatrix} - \phi_{S_n}(\mathbf{r}) \quad (34)$$

Weighted PCA is then applied on the vector

$$\boldsymbol{x}_S = \begin{bmatrix} \mathcal{D}[t_1(\cdot)] \\ \vdots \\ \mathcal{D}[t_n(\cdot)] \end{bmatrix} \quad (35)$$

with the weight

$$W = diag(W^{(1)}, W^{(1)} + W^{(2)}, \ldots, W^{(n-1)} + W^{(n)}) \quad (36)$$

to build the SSM.

2.6. Comparison of the shape representations

In this subsection, we compare the shape proposed and the three conventional shape representation methods mentioned above. Fig. 3 shows a one-dimensional illustration of the four shape representations. As we can see, RT-LSF can describe three nested shapes using a single function; however, it is not smooth at the boundary ∂S_2, as indicated by the blue arrows in Fig. 3(c), which may result in a nonlinear distribution of the training shapes and give negative influence on the performance of PCA.

Fig. 4 demonstrates the linear interpolation and extrapolation result between the two different nested circles $S = (S_1, S_2, S_3) \in \mathbb{T}_3$
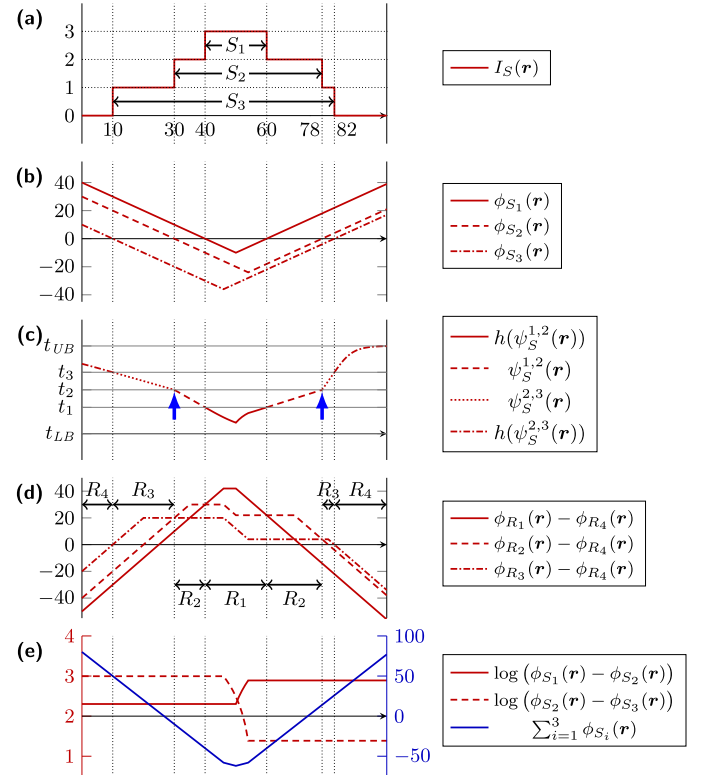

Fig. 3. A 1-D example of the conventional (a–d) and proposed (e) shape representations: (a) Discrete label representation (I_S) of the nested shapes (i.e., open intervals in the 1-D case) $S_1 = (40, 60)$, $S_2 = (30, 78)$, and $S_3 = (10, 82)$. (b) Signed distance functions (ϕ_{S_1}, ϕ_{S_2}, and ϕ_{S_3}) associated with each nested shape, which are employed by the multi-LSF method (Tsai et al., 2004). (c) RT-LSF method employed in (Saito et al., 2017), which describes nested shapes by applying different thresholds to a single continuous real-valued function. The slope of this function is not smooth at the boundary of S_2. (d) Functions of the logarithm of odds ratios (LogOdds) employed by Pohl et al. (2007). (e) Our LT-LSF method, which is based on the linear and logarithmic transformation of the signed distance functions.

and $S' = (S_1', S_2', S_3') \in \mathbb{T}_3$ using the different methods. The interpolation/extrapolation was carried out using the formula $(1 - t)\boldsymbol{x}_S + t\boldsymbol{x}_{S'}$, where $\boldsymbol{x}_S$ and $\boldsymbol{x}_{S'}$ are the shape representation vectors of S and S', respectively. While the intermediate shapes (see the column of $t = 0.5$) are similar between different methods and preserve an inclusive relationship, we found that the extrapolated shapes (see the columns of $t = -0.5$ and $t = 1.5$) are quite different depending on the method used. We also found that inclusive relationships were broken by extrapolation of the shape via multi-LSF and LogOdds (see the area indicated by the blue arrow in Fig. 4).

3. Experimental setup and results

The proposed method was demonstrated in the context of statistical shape modeling of the human embryonic brain surface, ventricle, and choroid plexus. These structures have a nesting relationship. The data was obtained from the Kyoto Collection of Human Embryos (Yamaguchi and Yamada, 2018), which is a large collection of human embryo and fetuses stored at the Congenital Anomaly Research Center of Kyoto University. We focused on 38 cases with Carnegie stages (CSs) of 20–23 that were selected based on our published criteria (Nakashima et al., 2012). For each case, the brain, ventricle, and choroid plexus labels were delineated on MR microscope volumes, which were acquired using T1-weighted spin echo sequences with a repetition time of 100 ms and an echo time of 10–16 ms in a system equipped with a 2.35-T/40-cm bore magnet (Matsuda et al., 2007). This study was approved by the
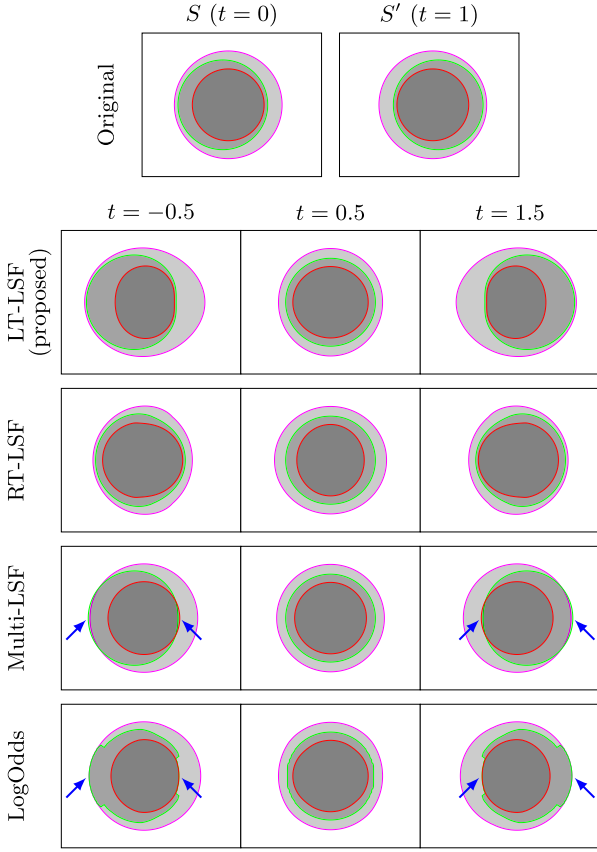
Fig. 4. Linear interpolation and extrapolation between two nested shapes. The top row shows the original nested shapes $S, S' \in \mathbb{T}_3$, which consist of three circles with radii 23, 29, and 35 centered at the points $(50 \pm 2, 50)$, $(50 \pm 6, 50)$, and $(50 \pm 2, 50)$, respectively. The second-to-last row shows the result of interpolation ($t = 0.5$) and extrapolation ($t = -0.5$, $t = 1.5$) between S and S' using the formula $(1 - t)\mathbf{x}_S + t\mathbf{x}_{S'}$, where $\mathbf{x}_S$ and $\mathbf{x}_{S'}$ are the shape descriptors associated with S and S', respectively.

Ethics Committee of the Graduate School and Faculty of Medicine at Kyoto University (R0316, R0989) and Tokyo University of Agriculture and Technology (approval no. 30-28).

Prior to statistical shape analysis, shape labels were aligned by generalized Procrustes analysis involving translation, rotation, and scaling using 21 automatically defined landmarks (Kasahara et al., 2017). The image size after alignment was $200 \times 250 \times 200$ with a 0.1 mm isotropic voxel size. The SSM was built by applying PCA on the discretized LSFs. The parameter for the weight was set as $\lambda = 0.09$ (cf. Eq. (14)) and $\gamma = 1.0$ [mm] (cf. Eq. (13)), which were optimized in an empirical manner based on the generalization performance. The number of principal components m was chosen so that the 90% of the cumulative contribution ratio was covered. To cover 90% of the variance, LT-LSF, RT-LSF, Multi-LSF, and LogOdds required $m = 6$ or $m = 7$ eigenmodes, while LDDMM required $m = 7$ to $m = 14$ eigenmodes, which means that the SSM using LDDMM is less compact (Styner et al., 2003) compared to the other SSMs.

The SSM by the proposed LT-LSF is compared with that by the methods we introduced in Section 2.5, i.e., RT-LSF (Saito et al., 2017), multi-LSF (Tsai et al., 2004), and LogOdds (Pohl et al., 2007). In addition, we compared our SSM with that based on diffeomorphic deformation of the shape template (Durrleman et al., 2014), which we will refer to as the large deformation diffeomorphic metric mapping (LDDMM)-based model. The deformation of the shape template in the LDDMM framework is represented as $I \circ \Phi_{\mathbf{q},\mu}^{-1}$. Here, I: $\Omega \to \{0, 1, 2, 3\}$ is the multi-valued label volume (cf. Fig. 3(a)), where each value indicates the background, brain tissue, ventricle, and choroid plexus, respectively, and $\Phi_{\mathbf{q},\mu}$: $\Omega \to \Omega$ represents the diffeomorphic transformation parameterized by n_{cp} control points $\mathbf{q} = (\mathbf{q}_1, \mathbf{q}_2, \ldots, \mathbf{q}_{n_{cp}})$ and moment vectors $\mu = (\mu_1, \mu_2, \ldots, \mu_{n_{cp}})$. The transformation $\Phi_{\mathbf{q},\mu}$: $\Omega \to \Omega$ is obtained by integrating the velocity field $\mathbf{v}_{\mathbf{q},\mu}(\mathbf{r})$ from $t = 0$ to $t = 1$:

$$\mathbf{v}_{\mathbf{q},\mu}(\mathbf{r}) = \sum_{i=1}^{n_{cp}} K(\mathbf{r}, \mathbf{q}_i) \cdot \mu_i \tag{37}$$

where $K(x, y)$ is a Gaussian kernel with a bandwidth of $\sigma = 2.0$ [mm]. We set $n_{cp} = 10 \times 10 \times 13 = 1300$ control points on the lattice in the image domain with an interval of σ, which was similar to the condition employed by Gori et al. (2017) ($n_{cp} = 1080$ with $\sigma = 7.0$ [mm]). To build the statistical shape model, groupwise registration based on ℓ_2-distance is performed among the training label volumes $\{I_S\}_{S \in \mathcal{T}_{train}}$ to obtain the geodesic mean (template) I and moment vectors $\{\mu^{(1)}, \mu^{(2)}, \ldots, \mu^{(m)}\}$ using the software `deformetrica`[2](Bône et al., 2018). PCA is then applied to the moment vectors to establish a parametric model.

The performance of SSM was evaluated by a two-fold cross-validation (CV) procedure, where 38 sets of nested shapes were randomly partitioned into two equal-sized subsets. The random partitioning was made such that each subset consists of the same number of cases for the same Carnegie stage. In order to obtain robust performance scores, random partitioning was repeated 100 times and 100 scores for different splittings were averaged. The performance of SSM was measured in terms of the *generalization* and *specificity* introduced by Styner et al. (2003). In addition, we introduce a *leakage* measure to assess the ability of the SSM to preserve the nesting relationships, i.e., $S_1 \Subset S_2 \Subset \cdots \Subset S_n$. First, let us define a similarity measure between two nested objects $S = (S_1, \ldots, S_n)$, $S' = (S'_1, \ldots, S'_n)$, which is defined as the sum of the Jaccard index

$$s(S, S') = \sum_{i=1}^{n} JI(S_i, S'_i) \tag{38}$$

where

$$JI(S_i, S'_i) = \frac{|S_i \cap S'_i|}{|S_i \cup S'_i|}. \tag{39}$$

Let $\mathcal{T}_{test} \subset \mathbb{S}$ be a set of unknown nested shapes and $\hat{S}$ denote the reconstruction of $S \in \mathcal{T}_{test}$ by the SSM. Generalization is then calculated as

$$\text{Generalization} = \frac{1}{|\mathcal{T}_{test}|} \sum_{S \in \mathcal{T}_{test}} s(S, \hat{S}) \tag{40}$$

which assesses the ability to reconstruct unknown shapes. To calculate specificity, we randomly generate a set of nested shape instances $\mathcal{R}$ from SSM using normal random numbers. We set the sampling number as $|\mathcal{R}| = 1,000$ at which calculated specificity had at most 0.007 of standard deviation, which is small enough to detect a statistically significant difference between the proposed and three conventional methods in this study. By averaging the highest similarity value between $S \in \mathcal{R}$ and the test shapes $\mathcal{T}_{test}$, we get

$$\text{Specificity} = \frac{1}{|\mathcal{R}|} \sum_{S' \in \mathcal{R}} \max_{S \in \mathcal{T}_{test}} s(S, S'). \tag{41}$$

Intuitively, this assesses whether the new instance generated by the SSM is acceptable. To evaluate whether the reconstructed

---

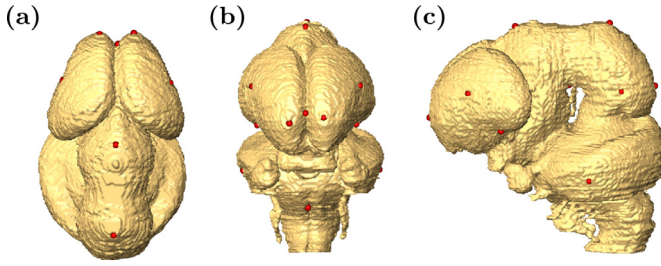[2] This software is available at http://www.deformetrica.org.

Fig. 5. An example of the automatically detected 21 landmarks on the brain surface with three different views: (a) top, (b) front, and (c) left.

shape $\hat{S}$ of $S \in \mathcal{T}_{\text{test}}$ and the randomly generated shape $S' \in \mathcal{R}$ preserve the nesting structure, we then provide the leakage measure. The leakage for a tuple of (possibly non-nested) shapes $S = (S_1, \ldots, S_n) \in \mathbb{S}^n$ is measured as the percentage of the area of the outer surface[3] ∂S_i belongs to the interior shape S_{i-1} or its surface ∂S_{i-1}.

$$Leak(S) = \frac{1}{n-1} \sum_{i=2}^{n} \frac{Area(\{\mathbf{r} \in \partial S_i | \phi_{S_{i-1}}(\mathbf{r}) \leq 0\})}{Area(\partial S_i)} \quad (42)$$

where $Area(\cdot)$ denotes the operation to calculate the surface area. The overall amount of leakage is measured in the process of calculation of generalization and specificity, which we refer to as leakage(G) and leakage(S), respectively, as follows:

$$Leakage(G) = \frac{1}{|\mathcal{T}_{\text{test}}|} \sum_{S \in \mathcal{T}_{\text{test}}} Leak(\hat{S}), \quad (43)$$

$$Leakage(S) = \frac{1}{|\mathcal{R}|} \sum_{S' \in \mathcal{R}} Leak(S'). \quad (44)$$

Clearly, we want these values to be zero.

Fig. 6(a) and (b) display the comparative results of the proposed method with the three conventional methods in terms of generalization and specificity abilities, respectively. The proposed SSM showed the highest performance on average. Statistical significance was tested for all the pairs between the proposed and the conventional methods using the Wilcoxon-signed rank test, under the null hypothesis that there is, on average, no difference between the two measurements. A statistically significant difference was observed for all the pairs at a significance level of $p = 0.01$. Fig. 6(c) displays the leakage values. We confirmed that multi-LSF and LogOdds had some leakage for both reconstructed shapes (cf. leakage(G)) and randomly generated shapes (cf. leakage(S)). The proposed method and RT-LSF did not have leakage, which was the theoretically expected result.

4. Discussions

The proposed SSM was superior to the previous ones in terms of both generalization and specificity with a statistically significant difference ($p < 0.01$). In addition, the proposed shape representation guarantees the inclusive relationship of the shape, which is a theoretical advantage over the multi-LSF (Tsai et al., 2004) and LogOdds (Pohl et al., 2007) methods, and this was confirmed by the fact that our SSM had no leakage. Thus, the proposed LT-LSF was the best shape representation among the five methods for representing nested surfaces of the embryonic brain.

Fig. 7 shows a typical example of the shape reconstruction results using different SSMs. The numerals show similarity indices
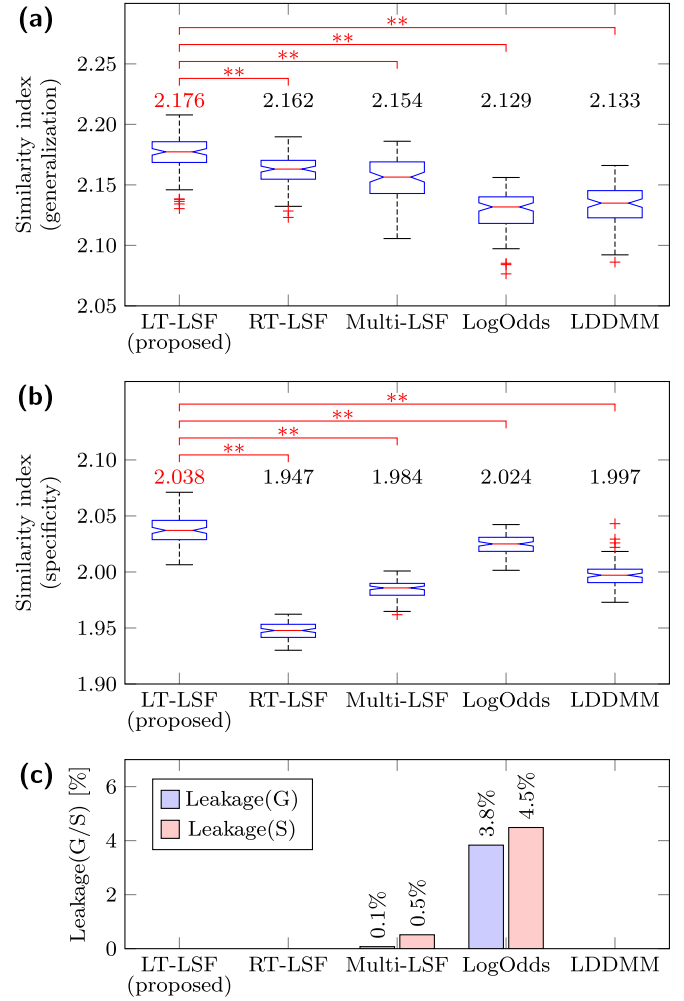
---

[3] The surfaces used to evaluate leakage were defined as triangular meshes generated by isosurfacing of the real-valued functions associated with each shape representation method. We employed the `isosurface` function in MATLAB R2017b for this procedure.

Fig. 6. Generalization (a), specificity (b), and leakage (c) measured for the five different SSMs. In (a) and (b), box plots show the distribution of the generalization (Eq. (40)) and specificity (Eq. (41)) for 100 different two-fold splits, and the numerals above the plots indicate the average values. A statistically significant difference between the proposed and all the other methods is also shown in these figures (**: $p < 0.01$).
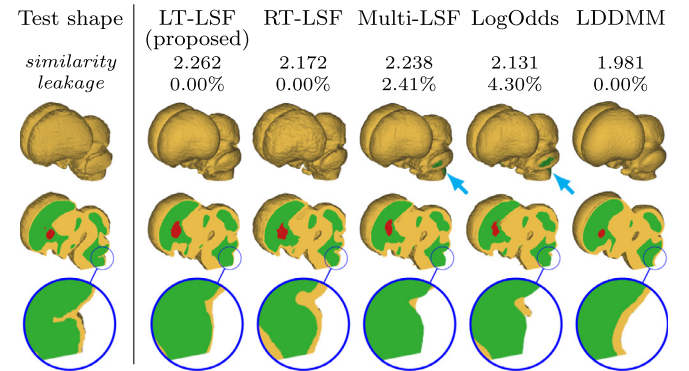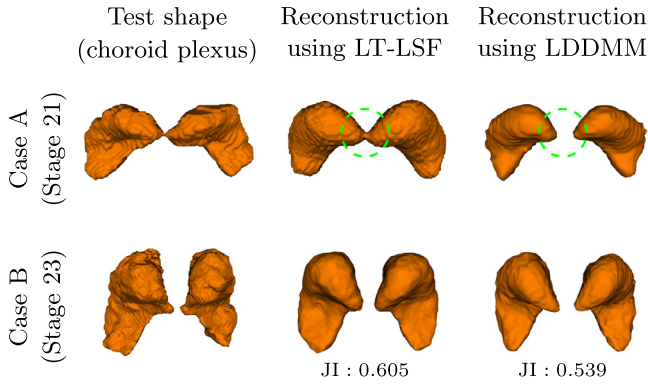

Fig. 7. Example of the reconstruction of the brain (yellow), ventricle (green), and choroid plexus (red) displayed using surface rendering (first row) and cross-sectioning (second row). From left to right, the input label volume is shown, followed by the reconstruction results of SSMs based on the proposed LT-LSF, RT-LSF, multi-LSF, LogOdds, and LDDMM. The numerals indicate similarity between the reconstructed shape and the original one. (For interpretation of the references to color in this figure caption, the reader is referred to the web version of this article.)

Fig. 8. Examples of the choroid plexus from Carnegie stages 21 and 23 (left column), and those reconstructed by the SSMs based on LT-LSF (middle column) and LDDMM (right column). The numerals below the figures indicate Jaccard indices between the test shapes and the reconstructed ones. Although cases A and B had different topology (connectivity), the proposed LT-LSF dealt with such topological changes, while LDDMM did not (see the areas inside the dotted circles).

(cf. Eq. (38)) and a higher value denotes better generalization. The proposed SSM showed the highest similarity value, which was consistent with the results from Fig. 6(a). One of the reasons that the proposed SSM had better reconstruction ability can be seen from the bottom row in Fig. 7. When using multi-LSF and LogOdds, the ventricle was protruded out of the brain surfaces where the two adjacent surfaces are close to each other. Fig. 8 briefly explains the advantage of the proposed LT-LSF over LDDMM in terms of the flexibility to topological change. The left and right of the choroid plexus of the human embryo tend to be spatially connected in the early developmental stage. The proposed method can handle such topological change, while LDDMM cannot due to the principle of the diffeomorphic deformation (cf. the green circle in Fig. 8).

Fig. 9 shows shapes from eigenshape spaces, which were generated from a uniform sampling of the first principal component score α_1 from -2σ to $+2\sigma$. We observed that when $\alpha_1 = -2\sigma$, SSM with RT-LSF had an irregularly shaped hollow on the forebrain (see the green arrow in Fig. 9), and such a shape was not observed in the training shape label (cf. Fig. 5). SSMs with multi-LSF and LogOdds generated shapes with leakage, i.e., the area of the surface of the ventricle came into contact with or protruded out of the brain surface (see the blue arrow in Fig. 9). Compared with the three conventional SSMs, the proposed one yielded more natural shapes, which might contribute to the improvement of specificity, as shown in Fig. 6(b).

Finally, we conclude the discussion by comparing the distribution of the shape representation on the eigenshape space. Fig. 10 compares the distribution of 38 training shapes between different shape representation methods using the scatter plot of the first three principal component scores. We found that an age-related feature was captured by the first principal mode. In principle, the distribution is desired to be Gaussian for higher performance in PCA. To evaluate the normality of the distribution quantitatively, we applied Henze–Zirkler's test[4] (Henze and Wagner, 1997) under the null hypothesis that "the population is normally distributed". We found that the proposed LT-LSF showed a higher p-value ($p = 0.008$) than the other methods, i.e., the normality was improved by using LT-LSF, which might be one reason for the higher generalization and specificity ability. However, the null hypothesis was rejected for all the methods with a significance level of $p = 0.01$, which suggests the existence of nonlinearity of the distribution of
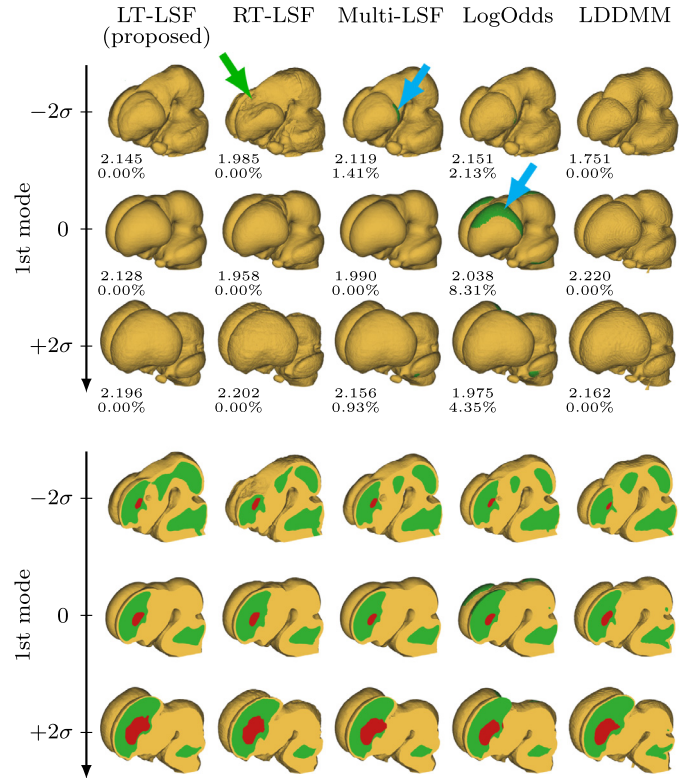
---

[4] This is the normality test for an arbitrary number of dimensions and has the desirable property of affine invariance. This test was applied on the space whose number of dimensions is chosen so that the cumulative contribution ratio is 90%.

Fig. 9. The first mode of $\pm$ 2 SD variations of the five SSMs displayed with external view (upper group) and sectional view (lower group). In each group, mean shapes are on the middle row. Numerals beside the shapes indicate the maximum similarity index $\max_{S \in \mathcal{T}_{\text{test}}} s(S, S')$ (cf. Eq. (41)) and the leakage $Leak(S')$ (cf. Eq. (44)) for each shape S'.
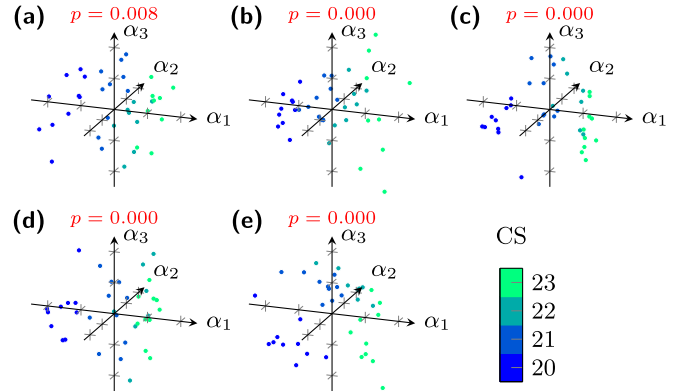

Fig. 10. Distribution of the 38 training data on the three dimensional latent space obtained from (a) LT-LSF, (b) RT-LSF, (c) multi-LSF, (d) LogOdds, and (e) LDDMM shape representations. We provided p-values of the Henze-Zirkler's test (Henze and Wagner, 1997) above the plots to indicate the normality of the distributions.

training features and nonlinear statistical analysis would achieve further improvement in the performance of SSM.

Conclusions

We proposed a multishape SSM for nested structures using a new shape representation method (LT-LSF) based on logarithmic transformation of level set functions, which was evaluated in the context of statistical shape modeling of brain, ventricle, and choroid plexus segmentation from noncontrast CT volumes of human embryos. The proposed method has the following notable features:

1. Our shape representation has a vector space structure equipped with closed operations with respect to the set of all the possible nested shapes, which ensures that the SSM preserves the correct nesting structure (leakage free), unlike the conventional methods (Tsai et al., 2004; Pohl et al., 2007). This fact was verified by our results.

2. Our method can be applied to an object with an arbitrary number of nested shapes.

3. The SSM with the proposed method achieved generalization and specificity values of 2.176 and 2.038, respectively, which outperformed the SSMs with conventional methods (Tsai et al., 2004; Pohl et al., 2007; Saito et al., 2017; Durrleman et al., 2014).

4. One possible reason behind the higher performance of our SSM is the higher normality of the distribution.

The main limitation of the proposed method is that it can only handle nested shapes. Development of an SSM for multiple objects including both nested shape pairs and non-overlapping shape pairs remains an ongoing research topic. In the future, we plan to develop a spatiotemporal SSM of the anatomy of the human embryo as well as SSM-based computer-aided diagnosis algorithms that include segmentation and assessment of the degree of abnormality. Other than human embryos, our method can be applied to any datasets including nested objects. Statistical shape modeling of endocardial and epicardial surfaces of the left ventricle (Carminati et al., 2018) and of outer and inner side of the cellular membrane (Vazquez-Reina et al., 2009) would be useful applications worth addressing in future work.

Conflict of interest

None.

Acknowledgment

Appendix A

Here, we give a proof for the fact that for any nested shapes $(S_1, \ldots, S_n) \in \mathbb{T}_n$, their signed distance function satisfies the inequality $\phi_{S_1}(\mathbf{r}) > \ldots > \phi_{S_n}(\mathbf{r}) \forall \mathbf{r} \in \Omega$. Because this proposition is equivalent to $(S_i, S_{i+1}) \in \mathbb{T}_2 \Rightarrow \phi_{S_i}(\mathbf{r}) > \phi_{S_{i+1}}(\mathbf{r}) \forall i \in \{1, \ldots, n-1\}$, we must prove the following corollary.

Corollary 1. *For $(S_1, S_2) \in \mathbb{T}_2$, the inequality $\phi_{S_1}(\mathbf{r}) > \phi_{S_2}(\mathbf{r})$ holds for any $\mathbf{r} \in \Omega$.*

Proof. It follows from Eq. (1) that

$$(\phi_{S_1}(\mathbf{r}), \phi_{S_2}(\mathbf{r}))$$
$$= \begin{cases} \left(-\min_{\mathbf{s} \in \partial S_1} \|\mathbf{r} - \mathbf{s}\|, -\min_{\mathbf{s} \in \partial S_2} \|\mathbf{r} - \mathbf{s}\| \right) & \text{if } \mathbf{r} \in S_1 \\ \left(\min_{\mathbf{s} \in \partial S_1} \|\mathbf{r} - \mathbf{s}\|, -\min_{\mathbf{s} \in \partial S_2} \|\mathbf{r} - \mathbf{s}\| \right) & \text{if } \mathbf{r} \in S_2 \setminus S_1 . \\ \left(\min_{\mathbf{s} \in \partial S_1} \|\mathbf{r} - \mathbf{s}\|, \min_{\mathbf{s} \in \partial S_2} \|\mathbf{r} - \mathbf{s}\| \right) & \text{if } \mathbf{r} \in \Omega \setminus S_2 \end{cases} \quad \text{(A.1)}$$

Let $\boldsymbol{n}_{S_i} = \arg\min_{\mathbf{s} \in \partial S_i} \|\mathbf{r} - \mathbf{s}\|$ be the point on ∂S_i that is closest to $\mathbf{r} \in \Omega$, and let $\ell_{S_i}(\mathbf{r})$ be a half-open line segment between $\mathbf{r}$ and $\boldsymbol{n}_{S_i}(\mathbf{r})$, i.e., $\ell_{S_i}(\mathbf{r}) = \{(s-1)\mathbf{r} + s\boldsymbol{n}_{S_i}(\mathbf{r}) \mid s \in [0, 1)\}$. If $\mathbf{r} \in S_1$, because $\boldsymbol{n}_{S_2}(\mathbf{r}) \notin S_1$ ($\because S_1 \cap \partial S_2 = \emptyset$), the line $\ell_{S_2}(\mathbf{r})$ and the contour ∂S_1 always have at least one intersection point $\boldsymbol{z} \in \ell_{S_2}(\mathbf{r}) \cap \partial S_1$ (see Fig. A.1(a)). Since $\boldsymbol{z}$ is closer to $\mathbf{r}$ than $\boldsymbol{n}_{S_2}(\mathbf{r})$, we have
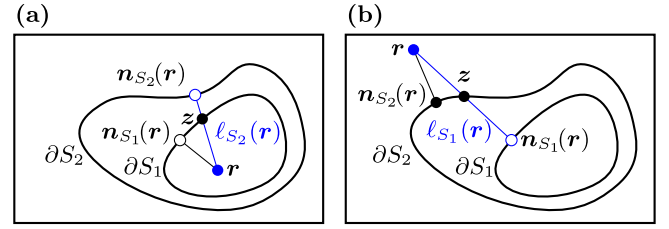

(a)   (b)

Fig. A1. Illustration used in the proof of Corollary 1.

$\|\mathbf{r} - \boldsymbol{n}_{S_2}(\mathbf{r})\| > \|\mathbf{r} - \boldsymbol{z}\|$. Using this, we have the following inequality:

$$\|\mathbf{r} - \boldsymbol{n}_{S_2}(\mathbf{r})\| > \|\mathbf{r} - \boldsymbol{z}\| \geq \|\mathbf{r} - \boldsymbol{n}_{S_1}(\mathbf{r})\| \quad \forall \mathbf{r} \in S_1. \quad \text{(A.2)}$$

Therefore, we have

$$\phi_{S_1}(\mathbf{r}) \equiv -\min_{\mathbf{s} \in \partial S_1} \|\mathbf{r} - \mathbf{s}\|$$
$$> -\min_{\mathbf{s} \in \partial S_2} \|\mathbf{r} - \mathbf{s}\| \equiv \phi_{S_2}(\mathbf{r}) \quad \forall \mathbf{r} \in S_1 \quad \text{(A.3)}$$

As before, if $\mathbf{r} \in \Omega \setminus S_2$, because $\boldsymbol{n}_{S_1}(\mathbf{r}) \notin \Omega \setminus S_2$ ($\because (\Omega \setminus S_2) \cap \partial S_1 = \emptyset$), the line ℓ_{S_1} and the contour ∂S_2 always have at least one intersection point $\boldsymbol{z} \in \ell_{S_1}(\mathbf{r}) \cap \partial S_2$ (see Fig. A.1(b)). Consequently,

$$\|\mathbf{r} - \boldsymbol{n}_{S_1}(\mathbf{r})\| > \|\mathbf{r} - \boldsymbol{z}\| \geq \|\mathbf{r} - \boldsymbol{n}_{S_2}(\mathbf{r})\| \quad \forall \mathbf{r} \in \Omega \setminus S_2. \quad \text{(A.4)}$$

Therefore, we have

$$\phi_{S_1}(\mathbf{r}) \equiv \min_{\mathbf{s} \in \partial S_1} \|\mathbf{r} - \mathbf{s}\|$$
$$> \min_{\mathbf{s} \in \partial S_2} \|\mathbf{r} - \mathbf{s}\| \equiv \phi_{S_2}(\mathbf{r}) \quad \forall \mathbf{r} \in \Omega \setminus S_2. \quad \text{(A.5)}$$

If $\mathbf{r} \in S_2 \setminus S_1$, then from the definition in Eq. (A.1), we have

$$\phi_{S_1}(\mathbf{r}) \equiv \min_{\mathbf{s} \in \partial S_1} \|\mathbf{r} - \mathbf{s}\| \geq 0, \quad \text{(A.6)}$$

$$\phi_{S_2}(\mathbf{r}) \equiv -\min_{\mathbf{s} \in \partial S_2} \|\mathbf{r} - \mathbf{s}\| < 0. \quad \text{(A.7)}$$

Equality in Eq. (A.6) is because S_1 is an open set and $S_2 \setminus S_1$ includes the boundary ∂S_1. From Eqs. (A.6) and (A.6), we get

$$\phi_{S_1}(\mathbf{r}) > \phi_{S_2}(\mathbf{r}) \quad \forall \mathbf{r} \in S_2 \setminus S_1. \quad \text{(A.8)}$$

Finally, from Eqs. (A.3), (A.5), and (A.8), we get

$$\phi_{S_1}(\mathbf{r}) > \phi_{S_2}(\mathbf{r}) \quad \forall (S_1, S_2) \in \mathbb{T}_2, \forall \mathbf{r} \in \Omega.$$

□

Then, we prove that the inequality $\varphi_1(\mathbf{r}) > \ldots > \varphi_n(\mathbf{r}) \forall \mathbf{r} \in \Omega$ is the sufficient condition for their sublevel sets being nested, i.e., $(S_1, \ldots, S_n) \in \mathbb{T}_n$, where we denote $\varphi_i : \Omega \to \mathbb{R}$ as the ith continuous real-valued function and $S_i = \{\mathbf{r} \in \Omega | \varphi_i(\mathbf{r}) < 0\}$ as the corresponding sublevel set. As before, because this proposition can be decomposed as $\varphi_i(\mathbf{r}) > \varphi_{i+1}(\mathbf{r}) \Rightarrow (S_i, S_{i+1}) \in \mathbb{T}_2 \forall i \in \{1, \ldots, n-1\}$, we consider the following corollary:

Corollary 2. *If the two real-valued functions $\varphi_1, \varphi_2 : \Omega \to \mathbb{R}$ are the continuous functions and satisfy $\varphi_1(\mathbf{r}) > \varphi_2(\mathbf{r}) \forall \mathbf{r} \in \Omega$, then $S_1 = \{\mathbf{r} \in \Omega \mid \varphi_1(\mathbf{r}) < 0\}$ and $S_2 = \{\mathbf{r} \in \Omega \mid \varphi_2(\mathbf{r}) < 0\}$ are the nested shapes, i.e., $S_1 \Subset S_2$.*

Proof. Since $\varphi_1(\mathbf{r}) > \varphi_2(\mathbf{r}) \quad \forall \mathbf{r} \in \Omega$, any point $\mathbf{r} \in \Omega$ satisfying $\varphi_1(\mathbf{r}) < 0$ always satisfies $\varphi_2(\mathbf{r}) < 0$, which means $\mathbf{r} \in S_2$ holds for all $\mathbf{r} \in S_1$. Therefore, we have $S_1 \subset S_2$. Then, to state that $S_1 \Subset S_2$ is true, we must prove $\partial S_1 \cap \partial S_2 = \emptyset$. Since φ_1 and φ_2 are continuous functions, we have $\partial S_1 = \{\mathbf{r} \in \Omega \mid \varphi_1(\mathbf{r}) = 0\}$ and $\partial S_2 = \{\mathbf{r} \in \Omega \mid \varphi_2(\mathbf{r}) = 0\}$. Finally, from the assumption that $\varphi_1(\mathbf{r}) > \varphi_2(\mathbf{r}) \forall \mathbf{r} \in \Omega$, we get $\partial S_1 \cap \partial S_2 = \{\mathbf{r} \in \Omega \mid \varphi_1(\mathbf{r}) = \varphi_2(\mathbf{r}) = 0\} = \emptyset$. □

References

Bône, A., Louis, M., Martin, B., Durrleman, S., 2018. Deformetrica 4: an open–source software for statistical shape analysis. In: Reuter, M., Wachinger, C., Lombaert, H., Paniagua, B., Lüthi, M., Egger, B. (Eds.), Shape in Medical Imaging. Springer International Publishing, Cham, pp. 3–13.

Carminati, M., Piazzese, C., Pepi, M., Tamborini, G., Gripari, P., Pontone, G., Krause, R., Auricchio, A., Lang, R., Caiani, E., 2018. A statistical shape model of the left ventricle from real-time 3D echocardiography and its application to myocardial segmentation of cardiac magnetic resonance images. Comput. Biol. Med. 96, 241–251. doi:10.1016/j.compbiomed.2018.03.013.

Changizi, N., Hamarneh, G., 2010. Probabilistic multi-shape representation using an isometric log-ratio mapping. In: Jiang, T., Navab, N., Pluim, J.P.W., Viergever, M.A. (Eds.), MICCAI 2010. LNCS, vol. 6363. Springer, Heidelberg, pp. 563–570. doi:10.1007/978-3-642-15711-0_70.

Chung, G., Vese, L.A., 2009. Image segmentation using a multilayer level-set approach. Comput. Vis. Sci. 12 (6), 267–285. doi:10.1007/s00791-008-0113-1.

Cootes, T.F., Taylor, C.J., Cooper, D.H., Graham, J., 1995. Active shape models-their training and application. Comput. Vis. Image Underst. 61 (1), 38–59. doi:10.1006/cviu.1995.1004.

Cremers, D., Rousson, M., Deriche, R., 2007. A review of statistical approaches to level set segmentation: integrating color, texture, motion and shape. Int. J. Comput. Vis. 72 (2), 195–215. doi:10.1007/s11263-006-8711-1.

Durrleman, S., Prastawa, M., Charon, N., Korenberg, J.R., Joshi, S., Gerig, G., Trouvé, A., 2014. Morphometry of anatomical shape complexes with dense deformations and sparse parameters. NeuroImage 101, 35–49. doi:10.1016/j.neuroimage.2014.06.043.

Duta, N., Sonka, M., 1998. Segmentation and interpretation of MR brain images. an improved active shape model. IEEE Trans. Med. Imaging 17 (6), 1049–1062. doi:10.1109/42.746716.

Fishbaugh, J., Durrleman, S., Prastawa, M., Gerig, G., 2017. Geodesic shape regression with multiple geometries and sparse parameters. Med. Image Anal. 39, 1–17. doi:10.1016/j.media.2017.03.008.

Frangi, A.F., Rueckert, D., Schnabel, J.A., Niessen, W.J., 2002. Automatic construction of multiple-object three-dimensional statistical shape models: application to cardiac modeling. IEEE Trans. Med. Imaging 21 (9), 1151–1166. doi:10.1109/tmi.2002.804426.

Gori, P., Colliot, O., Marrakchi-Kacem, L., Worbe, Y., Poupon, C., Hartmann, A., Ayache, N., Durrleman, S., 2017. A Bayesian framework for joint morphometry of surface and curve meshes in multi-object complexes. Med. Image Anal. 35, 458–474. doi:10.1016/j.media.2016.08.011.

Heimann, T., Meinzer, H.-P., 2009. Statistical shape models for 3D medical image segmentation: a review. Med. Image Anal. 13 (4), 543–563. doi:10.1016/j.media.2009.05.004.

Henze, N., Wagner, T., 1997. A new approach to the bhep tests for multivariate normality. J. Multivar. Anal. 62 (1), 1–23. doi:10.1006/jmva.1997.1684.

Hormander, L., 1973. An Introduction to Complex Analysis in Several Variables, 7. Elsevier.

Jing, Y., Staib, L.H., Duncan, J.S., 2004. Neighbor-constrained segmentation with level set based 3-D deformable models. IEEE Trans. Med. Imaging 23 (8), 940–948. doi:10.1109/TMI.2004.830802.

Kasahara, K., Saito, A., Takakuwa, T., Yamada, S., 2017. A spatiotemporal statistical shape model of brain surface during human embryonic development. In: Proceedings of International Forum on Medical Imaging in Asia (IFMIA) 2017, pp. 282–284.

Liu, Y., Captur, G., Moon, J.C., Guo, S., Yang, X., Zhang, S., Li, C., 2016. Distance regularized two level sets for segmentation of left and right ventricles from cine-MRI. Magn. Reson. Imaging 34 (5), 699–706. doi:10.1016/j.mri.2015.12.027.

Malcolm, J., Rathi, Y., Shenton, M.E., Tannenbaum, A., 2008. Label space: a coupled multi-shape representation. In: Metaxas, D., Axel, L., Fichtinger, G., Székely, G.

(Eds.), MICCAI 2008. LNCS, vol. 5242. Springer, Heidelberg, pp. 416–424. doi:10.1007/978-3-540-85990-1_50.

Matsuda, Y., Ono, S., Otake, Y., Handa, S., Kose, K., Haishi, T., Yamada, S., Uwabe, C., Shiota, K., 2007. Imaging of a large collection of human embryo using a super-parallel MR microscope. Magn. Reson. Med. Sci. 6 (3), 139–146. doi:10.2463/mrms.6.139.

Nakashima, T., Hirose, A., Yamada, S., Uwabe, C., Kose, K., Takakuwa, T., 2012. Morphometric analysis of the brain vesicles during the human embryonic period by magnetic resonance microscopic imaging. Congenit. Anom. 52 (1), 55–58. doi:10.1111/j.1741-4520.2011.00345.x.

Okada, T., Linguraru, M.G., Hori, M., Summers, R.M., Tomiyama, N., Sato, Y., 2015. Abdominal multi-organ segmentation from CT images using conditional shape-location and unsupervised intensity priors. Med. Image Anal. 26 (1), 1–18. doi:10.1016/j.media.2015.06.009.

Pizer, S.M., Jung, S., Goswami, D., Vicory, J., Zhao, X., Chaudhuri, R., Damon, J.N., Huckemann, S., Marron, J., 2013. Nested sphere statistics of skeletal models. In: Innovations for Shape Analysis. Springer, pp. 93–115.

Pohl, K.M., Fisher, J., Bouix, S., Shenton, M., McCarley, R.W., Grimson, W.E.L., Kikinis, R., Wells, W.M., 2007. Using the logarithm of odds to define a vector space on probabilistic atlases. Med. Image Anal. 11 (5), 465–477. doi:10.1016/j.media.2007.06.003.

Saito, A., Nakada, M., Oost, E., Shimizu, A., Watanabe, H., Nawano, S., 2013. A statistical shape model for multiple organs based on synthesized-based learning. In: Yoshida, H., Warfield, S., Vannier, M.W. (Eds.), ABD-MICCAI 2013. LNCS, vol. 8198. Springer, Berlin, Heidelberg, pp. 280–289. doi:10.1007/978-3-642-41083-3_31.

Saito, A., Tsujikawa, M., Takakuwa, T., Yamada, S., Shimizu, A., 2017. Statistical shape model of nested structures based on the level set. In: Descoteaux, M., Maier-Hein, L., Franz, A., Jannin, P., Collins, D.L., Duchesne, S. (Eds.), MICCAI 2017. LNCS, vol. 10433. Springer, Cham, pp. 169–176. doi:10.1007/978-3-319-66182-7_20.

Saito, T., Toriwaki, J.-I., 1994. New algorithms for euclidean distance transformation of an n-dimensional digitized picture with applications. Pattern Recognit. 27 (11), 1551–1565. doi:10.1016/0031-3203(94)90133-3.

Styner, M.A., Rajamani, K.T., Nolte, L.-P., Zsemlye, G., Székely, G., Taylor, C.J., Davies, R.H., 2003. Evaluation of 3D correspondence methods for model building. In: Taylor, C., Noble, J.A. (Eds.), IPMI 2003. LNCS, vol. 2732. Springer, Berlin, Heidelberg, pp. 63–75. doi:10.1007/978-3-540-45087-0_6.

Tsai, A., Wells, W., Tempany, C., Grimson, E., Willsky, A., 2004. Mutual information in coupled multi-shape model for medical image segmentation. Med. Image Anal. 8 (4), 429–445. doi:10.1016/j.media.2004.01.003.

Uchida, Y., Shimizu, A., Kobatake, H., Nawano, S., Shinozaki, K., 2010. A comparative study of statistical shape models of the pancreas. In: Computer Assisted Radiology and Surgery, 5, pp. S385–S387.

Vazquez-Reina, A., Miller, E., Pfister, H., 2009. Multiphase geometric couplings for the segmentation of neural processes. In: 2009 IEEE Conference on Computer Vision and Pattern Recognition, pp. 2020–2027. doi:10.1109/CVPR.2009.5206524.

Wang, H., Stout, D.B., Chatziioannou, A.F., 2012. Estimation of mouse organ locations through registration of a statistical mouse atlas with micro-CT images. IEEE Trans. Med. Imaging 31 (1), 88–102. doi:10.1109/TMI.2011.2165294.

Yamaguchi, Y., Yamada, S., 2018. The Kyoto collection of human embryos and fetuses: history and recent advancements in modern methods. Cells Tissues Organs doi:10.1159/000490672.

Yang, C., Wu, W., Su, Y., Zhang, S., 2017. Left ventricle segmentation via two-layer level sets with circular shape constraint. Magn. Reson. Imaging 38, 202–213. doi:10.1016/j.mri.2017.01.011.

Yushkevich, P., Thomas Fletcher, P., Joshi, S., Thall, A., Pizer, S.M., 2003. Continuous medial representations for geometric object modeling in 2D and 3D. Image Vis. Comput. 21 (1), 17–27. doi:10.1016/S0262-8856(02)00135-X.